# Glassy Phonon Heralds a Strain Glass State in a Shape Memory Alloy

P. J. Stonaha,[1,*] I. Karaman,[2] R. Arroyave,[2,3] D. Salas,[2] N. M. Bruno,[2] Y. Wang,[3] M. F. Chisholm,[1] S. Chi,[4] D. L. Abernathy,[4] Y. I. Chumlyakov,[5] and M. E. Manley[1,†]

[1]*Material Science and Technology Division, Oak Ridge National Lab, Oak Ridge, Tennessee 37831, USA*
[2]*Department of Material Science and Engineering, Texas A&M University, College Station, Texas 77843, USA*
[3]*Department of Mechanical Engineering, Texas A&M University, College Station, Texas 77843, USA*
[4]*Neutron Scattering Division, Oak Ridge National Lab, Oak Ridge, Tennessee 37831, USA*
[5]*Siberian Physical Technical Institute, Tomsk State University, Tomsk, 634050, Russia*

(Received 4 December 2017; revised manuscript received 30 March 2018; published 11 June 2018)

Shape memory strain glasses are frustrated ferroelastic materials with glasslike slow relaxation and nanodomains. It is possible to change a NiCoMnIn Heusler alloy from a martensitically transforming alloy to a nontransforming strain glass by annealing, but minimal differences are evident in the short- or long-range order above the transition temperature—although there is a structural relaxation and a 0.18% lattice expansion in the annealed sample. Using neutron scattering we find glasslike phonon damping in the strain glass but not the transforming alloy at temperatures well above the transition. Damping occurs in the mode with displacements matching the martensitic transformation. With support from first-principles calculations, we argue that the strain glass originates not with transformation strain pinning but with a disruption of the underlying electronic instability when disorder resonance states cross the Fermi level.

DOI: 10.1103/PhysRevLett.120.245701

Materials exhibiting phase instabilities are important for many emerging technologies. These include $VO_2$, where a metal-insulator transition enables its use in smart windows [1], relaxor-based ferroelectric materials with uses in actuators and sensors [2], and shape memory alloys, which are the focus of this work and have a diverse range of applications ranging from medical devices to fashion accessories [3–5]. The shape memory effect is a result of the first-order diffusionless martensitic transformation in which the high-temperature parent phase transforms into a lower symmetry crystal structure under a change in temperature, stress, or magnetic field [6]. The lattice instability associated with the martensitic transformation manifests as the softening of the transverse acoustic ($TA_2$) phonon, which is observed in many shape memory alloys near the wave vector $q = [\frac{1}{3}, \frac{1}{3}, 0]$ [7–11].

A strain glass is identified by a frequency-dependent anomaly in the ac mechanical susceptibility, a nonergodic mechanical response, average crystal order matching the parent phase, and short-range strain ordering [12]. The strain glass state was first discovered in 2005 in the shape memory alloy NiTi under excess Ni doping (1%–2%). The authors proposed that the strain glass state arises from a critical amount of disorder that pins random strain regions of nanoscale dimension throughout the material, while leaving the average structure unchanged [13]. Since the discovery of the first strain glass, several others have been discovered in off-stoichiometric compositions of shape memory alloys [14,15] and in materials that normally undergo martensitic transformations.

We address the magnetic Heusler alloy $Ni_{45}Co_5Mn_{36.6}In_{13.4}$ (NCMI). When quenched from a solution heat treatment temperature ($T > 896$ K), this material forms a metamagnetic shape memory alloy comprising mostly $B2$ crystal order [16], in which Mn and In share one sublattice and Ni and Co share the other sublattice. A small volume fraction of the quenched sample comprises domains of the $L2_1$ ordered state, where In is restricted to the $4b$ positions [cf. Fig. 1(a)]. Subjecting the crystal to a secondary heat treatment (500 K $< T <$ 900 K) promotes growth of $L2_1$ domains [16] and alters the martensitic transformation temperature ($T_M$). After a secondary heat treatment (3 h at 573 K, followed by quenching), the martensitic transformation in NCMI is completely arrested [17], and the crystal enters a strain glass state when cooled below the strain glass temperature ($T_g = 104$ K) [18]. The strain glass transition is fully reversible, with the sample recovering the unstrained parent phase when reheated to temperatures well above $T_g$. Here, we study the lattice dynamics of two samples of NCMI—one prepared as a shape memory alloy and the other prepared as a strain glass. Our results show that strain glass behavior does not originate with the pinning of random strains, as assumed [13], but with a disruption of the underlying electronic instability.

We denote the sample that was (was not) subjected to a secondary heat treatment as the "strain glass" ("shape memory alloy") [19]. The temperature-dependent magnetizations of the samples are shown in Fig. 1(b). The Curie temperature for both samples is near $T_C = 400$ K. The

 

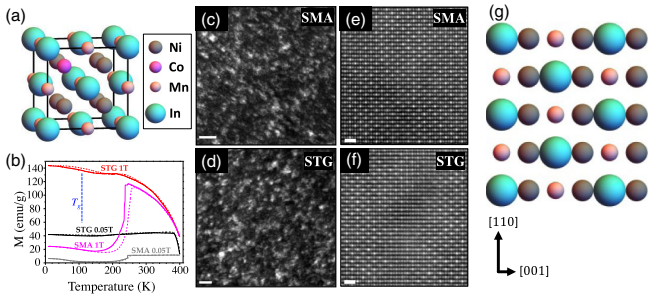


FIG. 1. Electron microscopy used to characterize the structure of our NCMI samples. (a) Heusler $L2_1$ crystal structure (space group $Fm\bar{3}m$). One Ni has been substituted with Co. In the $B2$ phase, the Mn and In atoms are randomly distributed on their sublattice. (b) Thermomagnetic response of the shape memory alloy (SMA) and strain glass (STG) samples during in field heating and in field-cooling under two different magnetic fields. Solid and dashed lines represent cooling and heating curves, respectively. The glass transition temperature ($T_g$) is indicated with the blue dashed line. (c)–(f), images of the two samples. The SMA and STG samples are shown in (c),(e) and (d),(f), respectively. (c),(d) Dark field image obtained using a (111) reflection from the $L2_1$ phase. The bright and dark regions have $L2_1$ and $B2$ ordering, respectively. The scale bars are 20 nm. (e), (f) High magnification high angle annular dark field STEM images along the $[1\bar{1}0]$ axis, with the [001] axis horizontal. The scale bars are 6 Å. The blurry region near the center in (f) is an antiphase domain boundary. There is no correspondence between the regions of the sample imaged in (e) and (c) or (f) and (d). (g) Depiction of the crystal structure along the viewing axis in (e), (f). No Co atoms are included in this projection.

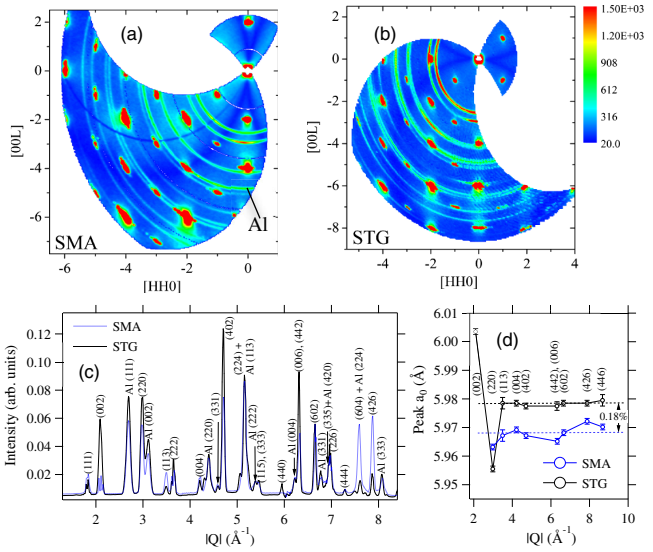


FIG. 2. Time-of-flight (ARCS) neutron scattering measurements used to characterize the diffraction and diffuse elastic scattering of our NCMI samples. (a),(b) Elastic scattering intensity measured in the plane for the shape memory alloy (SMA) and strain glass (STG). The rings (indicated Al) are aluminum powder diffraction rings from the crystal holder. The superlattice reflections are those with odd indices [e.g., (115)]. (c) Partial powder patterns obtained by integrating the elastic [$E = (0 \pm 1)$ meV] scattering over the entire volume sampled in the ARCS measurement for both the SMA and STG. These data include diffraction peaks from both in the plane [shown in (a),(b)] and about a Brillouin zone above and below the plane. Both (111) peaks and the SMA (002) peak appear as noise because the high intensity saturated the detector tubes on ARCS. (d) Apparent lattice parameter, $a_0$, deduced from the positions of the diffraction peaks indicated. The Al diffraction was used to calibrate the instrument.

shape memory alloy shows another magnetic transition around 230 K where the sample undergoes its first-order martensitic transformation. In contrast, the strain glass evidences no magnetic transition.

Electron microscopy images from both samples are shown in Figs. 1(c)–1(f) [19]. The low magnification images [Figs. 1(c) and 1(d)] are transmission electron microscope (TEM) dark field images obtained using a (111) reflection from the $L2_1$ phase. The light regions in these images are $L2_1$ domains in the dark the $B2$ matrix. It is important to note that the ordering observed in dark field images is an average through the thickness of the TEM sample. The high magnification images [Figs. 1(e) and 1(f)] are scanning TEM (STEM) images, taken along $[1\bar{1}0]$ with [110] directed upwards in the image. In this projection, the bright features in the image are the result of scattering from columns composed indium, manganese, and nickel (with cobalt). A depiction of the $L2_1$ structure viewed along this projection is shown in Fig. 1(g). We find no dramatic differences between the electron microscopy images of the two samples that can account for the incipient strain glass state.

Making use of the elastic scattering in the time-of-flight neutron scattering, we look for subtle structural differences that may have been missed by electron microscopy. Figures 2(a) and 2(b), show the elastic scattering in the (HHL) plane. After accounting for differences in neutron absorption by the samples there is no difference in the ratio of the superlattice to primary peak intensities (within ~5% uncertainty)—indicating a similar degree of chemical ordering. This is consistent with the microscopy images shown in Figs. 1(c) and 1(d). The diffuse elastic scattering, which is consistent with the presence of anti-phase boundaries [cf. Fig. 1(f)], also does not change by more than 5%. Diffraction peaks obtained by integrating the full data set appear broad [cf. Fig. 1(c)] because of the low $Q$ resolution of the ARCS instrument, making it impractical to characterize strain or size broadening. However, most of the peak positions are well determined. As can be seen in Fig. 2(d) the differences between the SMA and STG samples are peak shifts and an overall 0.18% expansion in the peak-dependent lattice parameters, $a_0$, in the STG sample.

We used inelastic neutron scattering to compare the lattice dynamics in the shape memory alloy and the strain glass [19]. Neutron scattering data from the $TA_2$ phonon in the shape memory alloy and strain glass collected using the HB3 triple-axis spectrometer are shown as constant-$\boldsymbol{Q}$ cuts

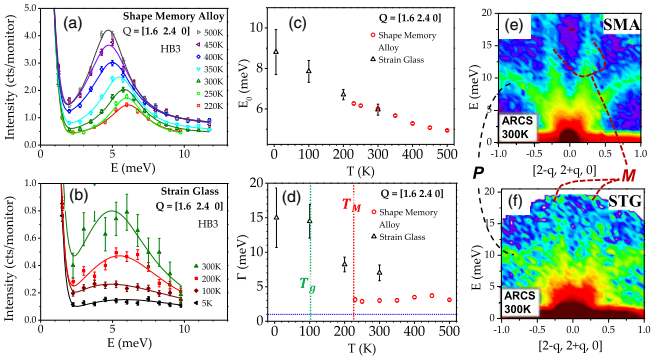


FIG. 3. Triple-axis (HB3) and time-of-flight (ARCS) inelastic neutron scattering measurements used to characterize the $TA_2$ phonon in our NCMI samples. (a),(b) Scattered neutron intensity along a constant-$\boldsymbol{Q}$ cut at $\boldsymbol{Q} = [1.6, 2.4, 0]$. The solid lines are fits using a thermally occupied damped harmonic oscillator plus an elastic peak. Error bars are statistical. (c),(d) Fit parameters for the lines in (a) and (b). $E_0$ is the bare phonon energy, and $\Gamma$ the FWHM. The dashed blue horizontal line in (d) represents the triple-axis instrument resolution, and the dashed red and green vertical lines represent the martensitic transformation temperature and the strain glass transition temperature, respectively. Error bars represent 1 s.d. (e), (f) Color plots of the scattered neutron intensity measured on the time-of-flight instrument from the shape memory alloy (SMA) and strain glass (STG). The intensity from the phonon ($P$) and magnon ($M$) are labeled accordingly. For clarity, only the phonons on the negative side of the origin are labeled.

at $q = 0.4$ reciprocal lattice units (r.l.u.) in Figs. 3(a) and 3(b). We fit these data to a thermally occupied damped harmonic oscillator plus an elastic peak. The fitted curves are overlaid in Figs. 3(a) and 3(b). No attempt was made to correct for the instrument resolution because the phonons are much broader than the resolution. Trends in the fitted bare phonon energy ($E_0$) and the full width half maximum linewidth (FWHM, $\Gamma$) are shown in Figs. 3(c) and 3(d). Constant-$\boldsymbol{Q}$ cuts made using data from ARCS show the same trends, ruling out any possible instrument-related artifacts [19]. Color plots of the scattered intensity measured using ARCS show that the broadening of the $TA_2$ phonon in the strain glass extends across the entire Brillouin zone [cf. Figs. 3(e) and 3(f)]. The steep features rising on either side of the (220) Bragg peak in Fig. 3(e) are the [110] magnon; when heated above $T_C$, these excitations vanish [19].

The stark difference in the width of the $TA_2$ phonons between the strain glass and shape memory NCMI samples reveals a large change in the interatomic potential energy landscape of the $TA_2$ phonon. The over-damping of the $TA_2$ phonon branch in the strain glass occurs over the entire reciprocal lattice zone, as shown in Fig. 3(e), indicating the damping extends all the way down to the atomic-scale shear displacements—defining what we call a "glassy phonon." This broadening is a signature of a highly anharmonic energy landscape which, in this case, likely results from a large number of nearly degenerate shear instabilities associated with displacements of the $TA_2$ phonon. As the crystal lattice absorbs the energy of a neutron to excite a $TA_2$ phonon, the lattice is quick to absorb the atomic displacements associated with the phonon. This likely occurs through a dynamic reconfiguration of the local strain and is a dynamic precursor to the strain glass state. STEM images from other strain glass systems have found dilute *static* lattice distortions at temperatures of $T_g + 150$ K [24,25]. However, the low concentration of lattice distortions in those systems—domains of diameter 3 nm separated by ~10 nm—would affect the phonon spectrum in NCMI within the region $q \leq 0.06$ r.l.u., which would be difficult to detect in an inelastic neutron scattering experiment.

The behavior of phonons is dictated at the most fundamental level by the material's electronic structure. All martensite structures of shape memory alloys ($L1_0$, $10M$, $14M$, etc.) appear as a shearing of approximately every three unit cells of the parent phase along [110], which has as its source a Fermi surface nesting vector near $q_F = [\frac{1}{3}, \frac{1}{3}, 0]$ within the alloys' electronic band structures [26]. Calculations indicate a change in magnetization and/or electronic density can disrupt the Fermi surface nesting [27]. In our case, the brief secondary heat treatment changes the lattice parameter, which alters the electronic structure in such a way to disperse the Fermi-surface-nesting wave vector across a range of length scales. This length-scale-distributed degenerate electronic structure translates in the dynamics to a broadening of the $TA_2$ phonon across the entire Brillouin zone.

To test if a change in the lattice parameter could shift the states toward the Fermi level, we performed first-principles electronic structure calculations as a function of lattice parameter [19]. Figure 4 shows that a sharp peak in the up-spin electronic density of states clearly shifts towards the Fermi level with an expansion of the lattice. This peak is dominated by the $d$-electron states of both Ni and Co. The Co randomly substitutes Ni on the Ni sublattice. Because Co is an impurity atom on the Ni sublattice, it is expected to form resonance (local) states. The formation of resonance electronic states from chemical disorder is an established concept [28], as is the connection between chemical disorder and electron band structure near the Fermi level [29]. Resonance states at the Fermi level will disrupt Fermi surface nesting because such localized states fill reciprocal space, including between nested Fermi surfaces.

Scattering from such resonant states should increase the electrical resistivity. To check this, we measured the resistivity of three additional NCMI samples, one prepared as a strain glass and two as shape memory alloys. These measurements show a 9% greater resistivity in the strain glass sample [19]. Resonant electron states may also exist in the shape memory alloy, but if the energy is not matched

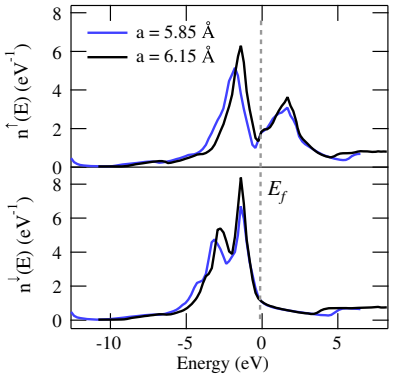


FIG. 4. Lattice expansion shifts electronic states towards the Fermi level ($E_f$) in the calculated electronic density of states of $Ni_{45}Co_5Mn_{36.6}In_{13.4}$ (NCMI). First-principles calculations were carried out using spin-polarized relativistic Korringa-Kohn-Rostoker (SPRKKR) band structure code [19]. The upper panel shows the spin-up states $[n\uparrow(E)]$ and the lower the spin-down states $[n\downarrow(E)]$.

to the Fermi level, the electrical resistivity of the shape memory alloy would be unaffected by the resonant states.

A transition to strain glass behavior can also be achieved by increasing the indium content in $Ni_{45}Co_5Mn_{50-x}In_x$ from $x = 3.4\%$ to $x = 13.9\%$ [30]. If the indium substitution disrupts the Fermi surface nesting by the same mechanism, then we would expect a similar lattice expansion. To check this, we performed first-principles calculations of the lattice parameter of $Ni_{45}Co_5Mn_{50-x}In_x$ as a function of both indium and degree of $L2_1$ order [19]. In the ordered state, there is a clear expansion of the lattice with increasing indium by 0.6% from $x = 13.3\%$ to 13.4% and then about 0.01% in going from $x = 13.4\%$ to 13.7% [19]. These changes are similar to the 0.18% expansion in going from our SMA to STG samples with annealing [cf. Fig. 2(d)], suggesting that lattice expansion plays a similar role in the development of strain glass behavior with increasing indium. An interesting implication is that it may be possible to reverse the phonon damping and strain glass state by reducing the lattice parameter with pressure.

The results presented herein show that the mechanism responsible for the strain glass state has a marked effect on the lattice dynamics at temperatures well above $T_g$ and $T_M$. At temperatures above $T_M$, the free energy favors the unstrained austenitic state in both samples [31,32]. If the frustration associated with the strain glass state were from strain pinning alone [13,33,34], then such strains would relax at such high temperatures, and we would see no evidence of frustration in the lattice dynamics at these temperatures. Thus, it seems inappropriate to discuss the strain glass state in terms of continuum concepts such as strain pinning, but instead consider how the state originates from the underlying electronic structure.

Research sponsored by the U.S. Department of Energy, Office of Basic Energy Sciences, Materials Sciences and Engineering Division. A portion of this research used resources at the High Flux Isotope Reactor and Spallation Neutron Source, a DOE Office of Science User Facility operated by the Oak Ridge National Laboratory. I. K., N. M. B., D. S., and R. A. acknowledge the financial support from the U.S. National Science Foundation, Division of Materials Research, Metals and Metallic Nanostructures Program, Grant No. 1508634.

*Present address: Department of Physics, Idaho State University, Pocatello, Idaho 83209, USA.
†manleyme@ornl.gov

[1] J. D. Budai, J. Hong, M. E. Manley, E. D. Specht, C. W. Li, J. Z. Tischler, D. L. Abernathy, A. H. Said, Bogdan M. Leu, L. A. Boatner, R. J. McQueeney, and O. Delaire, Nature (London) **515**, 535 (2014).
[2] M. E. Manley, D. L. Abernathy, R. Sahul, D. E. Parshall, J. W. Lynn, A. D. Christianson, P. J. Stonaha, E. D. Specht, and J. D. Budai, Sci. Adv. **2**, e1501814 (2016).
[3] N. B. Morgan, Mater. Sci. Eng. A **378**, 16 (2004).
[4] G. Song, N. Ma, and H. N. Li, Engineering structures **28**, 1266 (2006).
[5] J. Van Humbeeck, Mater. Sci. Eng. A **273–275**, 134 (1999).
[6] N. M. Bruno, S. Wang, I. Karaman, and Y. I. Chumlyakov, Sci. Rep. **7**, 40434 (2017).
[7] J. C. Lashley, S. M. Shapiro, B. Winn, C. P. Opeil, M. E. Manley, A. Alatas, W. Ratcliff, T. Park, R. A. Fisher, B. Mihaila, P. Riseborough, E. K. H. Salje, and J. L. Smith, Phys. Rev. Lett. **101**, 135703 (2008).
[8] X. Moya, L. Maños, A. Planes, T. Krenke, M. Acet, V. O. Garlea, T. A. Lograsso, D. L. Schlagel, and J. Zarestky, Phys. Rev. B **73**, 064303 (2006).
[9] X. Moya, D. Gonzalez-Alonso, L. Mañosa, A. Planes, V. O. Garlea, T. A. Lograsso, D. L. Schlagel, J. L. Zarestky, S. Aksoy, and M. Acet, Phys. Rev. B **79**, 214118 (2009).
[10] T. Ohba, S. Shapiro, S. Aoki, and K. Otsuka, Jap. J. Appl. Phys. **33**, L1631 (1994).
[11] S. M. Shapiro, B. X. Yang, G. Shirane, Y. Noda, and L. E. Tanner, Phys. Rev. Lett. **62**, 1298 (1989).
[12] X. Ren, Y. Wang, Y. Zhou, Z. Zhang, D. Wang, G. Fan, K. Otsuka, T. Suzuki, Y. Ji, J. Zhang, Y. Tian, S. Hou, and X. Ding, Philos. Mag. **90**, 141 (2010).
[13] S. Sarkar, X. Ren, and K. Otsuka, Phys. Rev. Lett. **95**, 205702 (2005).
[14] Y. M. Zhou, D. Z. Xue, X. D. Ding, K. Otsuka, J. Sun, and X. B. Ren, Appl. Phys. Lett. **95**, 151906 (2009).
[15] Z. Wu, Phys. Status Solidi RRL **9**, 317 (2015).
[16] W. Ito, M. Nagasako, R. Y. Umetsu, R. Kainuma, T. Kanomata, and K. Ishida, Appl. Phys. Lett. **93**, 232503 (2008).
[17] W. Ito, K. Ito, R. Y. Umetsu, R. Kainuma, K. Koyama, K. Watanabe, A. Fujita, K. Oikawa, K. Ishida, and T. Kanomata, Appl. Phys. Lett. **92**, 021908 (2008).
[18] J. A. Monroe, J. E. Raymond, X. Xu, M. Nagasako, R. Kainuma, Y. I. Chumlyakov, R. Arroyave, and I. Karaman, Acta Mater. **101**, 107 (2015).
[19] See Supplemental Material at http://link.aps.org/supplemental/10.1103/PhysRevLett.120.245701, which

includes Refs. [20–23], for a detailed description of the crystal preparation, electron microscopy, neutron scattering measurements, and additional supporting neutron scattering data showing TA broadening in the strain glass but not transforming alloy, the disappearance of magnon scattering above the Curie temperature, the absence of broadening in phonons not associated with the transition displacements, electrical resistivity measurements, and first-principles lattice parameter calculations.

[20] H. Ebert, D. Ködderitzsch, and J. Minár, Rep. Prog. Phys. **74**, 096501 (2011).

[21] H. Ebert, The munich spr-kkr package, version 6.3. URL: http://ebert.cup.uni-muenchen.de/SPRKKR.

[22] N. Singh, E. Dogan, I. Karaman, and R. Arróyave, Phys. Rev. B **84**, 184201 (2011).

[23] N. Singh and R. Arróyave, J. Appl. Phys. **113**, 183904 (2013).

[24] Y. Zhou, D. Xue, Y. Tian, X. Ding, S. Guo, K. Otsuka, J. Sun, and X. Ren, Phys. Rev. Lett. **112**, 025701 (2014).

[25] D. Schryvers, S. Cao, S. Pourbabak, H. Shi, and J. Lu, J. Alloys Compd. **577**, S705 (2013).

[26] C. Bungaro, K. M. Rabe, and A. Dal Corso, Phys. Rev. B **68**, 134104 (2003).

[27] M. Siewert, M. E. Gruner, A. Hucht, and H. C. Herper, Adv. Eng. Mater. **14**, 530 (2012).

[28] V. G. Karpov, Phys. Rev. B **48**, 4325 (1993).

[29] A. Borgschulte, D. Zur, D. Menzel, J. Schoenes, and P. M. Oppeneer, Phys. Rev. B **66**, 144421 (2002).

[30] X. Xu, W. Ito, R. Y. Umetsu, R. Kainuma, and K. Ishida, Appl. Phys. Lett. **95**, 181905 (2009).

[31] Z. Zhang, Y. Wang, D. Wang, Y. Zhou, K. Otsuka, and X. Ren, Phys. Rev. B **81**, 224102 (2010).

[32] J. Zhang, Y. Wang, X. Ding, Z. Zhang, Y. Zhou, X. Ren, D. Wang, Y. Ji, M. Song, K. Otsuka, and J. Sun, Phys. Rev. B **84**, 214201 (2011).

[33] D. Wang, D. Lv, Y. Gao, Y. Wang, X. Ren, and Y. Wang, J. Alloys Compd. **661**, 100 (2016).

[34] Y. Wang, C. Huang, J. Gao, S. Yang, X. Ding, X. Song, and X. Ren, Appl. Phys. Lett. **101**, 101913 (2012).